

Highly Mobile Excitons in Single Crystal Methylammonium Lead Tribromide Perovskite Microribbons

Luke McClintock,[†] Ziyi Song,[†] H. Clark Travaglini,[†] R. Tugrul Senger,^{‡,¶}
Vigneshwaran Chandrasekaran,[§] Han Htoon,[§] Dmitry Yarotski,[§] and Dong Yu[†]

[†]*Department of Physics, University of California-Davis, One Shields Avenue, Davis, CA
95616*

[‡]*Department of Physics, Izmir Institute of Technology, 35430 Izmir, Turkey*

[¶]*ICTP-ECAR Eurasian Center for Advanced Research, Izmir Institute of Technology,
35430 Izmir, Turkey*

[§]*Center for Integrated Nanotechnology, Los Alamos National Laboratory, Los Alamos, NM,
87545*

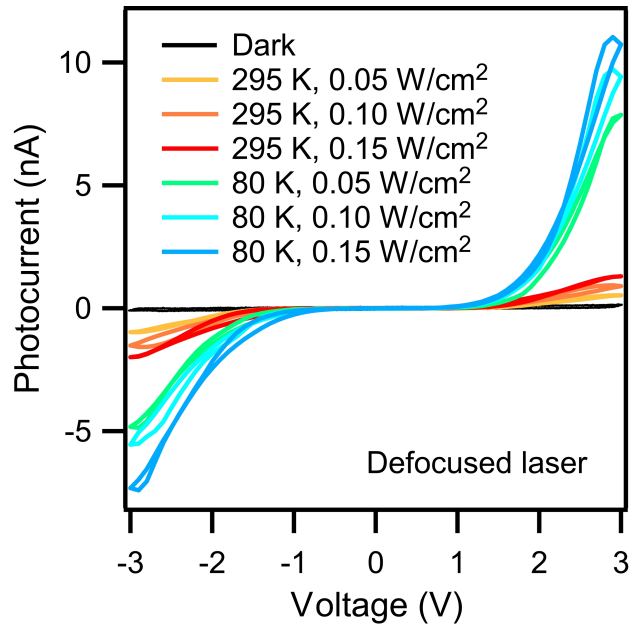


Figure S1: **Current-voltage curves.** Current vs. source-drain voltage curves at various global illumination intensities, at 295 K and 80 K, respectively. The nonlinear curves indicate a large contact barrier.

Elliott Fittings

The basic Elliott formula for an absorption spectrum can be written as

$$\alpha(\omega) = A \cdot \theta(\hbar\omega - E_g) \cdot \frac{\pi e^{\pi x}}{\sinh(\pi x)} + A \cdot R_{ex} \sum_{n_{ex}=1}^{\infty} \frac{4\pi}{n_{ex}^3} \cdot \delta(\hbar\omega - E_g + R_{ex}/n_{ex}^2) \quad (\text{S1})$$

where A is related to the interband transition matrix element, $\hbar\omega$ is the photon energy, θ is the Heaviside step-function, E_g is the bandgap energy, R_{ex} is the exciton Rydberg energy, n_{ex} is the principle quantum number, and x is defined to be $\sqrt{\frac{R_{ex}}{\hbar\omega - E_g}}$. Here, R_{ex} is equal to the exciton binding energy E_B when $n_{ex} = 1$.

Due to the nature of our data collection procedure (photocurrent rather than absorption), we expect the Elliott model to imperfectly handle the spectra fittings. We therefore interpret the output fitting parameters of E_B and E_g to be approximations, and attach error to their values by attempting the fit in more than one way. The inaccuracy of the fit at higher energies in the continuum is explained by the effects of Sommerfeld enhancement on the absorption coefficient, and is less interesting for our study. The convolved Elliott formula without a Sommerfeld term is expected to saturate at high energy, as shown in our plots, rather than continue to increase.

The interesting discrepancy between our experimental data and the model is what happens to the excitonic peak as temperature is decreased. The model predicts both the peak amplitude as well as the energy gap between peak and continuum to increase as E_B increases. In our data, we see this trend initially, but as temperature decreases and peak separation becomes more distinct, we do not see peak amplitude rise accordingly. By 140 K, the excitonic peak is clearly well-separated from the continuum edge, implying a large E_B , but the E_B value required to create this gap also calls for a much taller peak.

Therefore, we extract our E_B and E_g values by attempting to fit the spectra from the low and high energy sides of the peak, separately, as shown below (Fig S2). Fitting from the low energy side produced smaller E_B values while fitting from the high energy side produced

larger values. This makes sense, as the low energy side assumes the peak has been reached, whereas the high energy side tries to capture the gap between peak and continuum and does not know how high the peak reaches. This provides us with a form of minimum and maximum bound on the E_B , which we then average to give the values listed in the main text.

Furthermore, we can also make use of how well-resolved the peaks are from the continuum at low temperature. Since the gap between the peak center and the continuum edge is directly related to the E_B , we can look at the energy difference between peak center and half way up the continuum edge to get another estimate on the E_B . For example, at 110 K, the energy gap between the peak center and halfway up the continuum edge is about 38 meV, which agrees well with our fitting value. For the data collected between 80 K and 140 K, the error bars are set to reach between the min and max values of the fittings and are relatively small compared to higher temperatures due to the distinct separation of peak and continuum. For the data collected between 150 K and 300 K, the error bars are again set to reach between min and max values of the fittings but then additionally increased in proportion to temperature, since excitonic and continuum components begin to mix significantly as temperature increases.

The inaccuracy of the Elliott model at higher continuum energies is expected due to Sommerfeld enhancement of the absorption coefficient.¹ The extraction of E_B and the uncertainty estimation are detailed in Figure S2. As the excitonic peak grows and shifts with decreasing temperature, binding energies appear to increase while bandgap energy decreases. Two structural phase changes occur across this range of temperatures, the cubic to tetragonal transition at about 235 K, and the larger (in terms of lattice distortion) tetragonal to orthorhombic transition around 145 K.² E_B grows steadily until the first change, where it then stagnates around 34 meV. It then abruptly jumps to about 39 meV at the second phase change, simultaneous with a sharp blueshift in E_g . We have thus far found no other report showing spectral behavior with such clear separation of excitonic and continuum compo-

nents for halide perovskites. Interestingly, the Elliott fittings begin to fail as temperature decreases, since the Elliott model predicts the exciton peak to grow in amplitude, relative to the continuum, as separation from the continuum edge (and therefore E_B) increases (see Supporting Information). In the data, however, the peak amplitude increases at first but then begins to decrease (Figure 1f), which can be understood by the difficulty of splitting excitons at the contact. This deviation from the Elliott model can be related to our spectra being obtained via photocurrent, rather than via optical absorption.

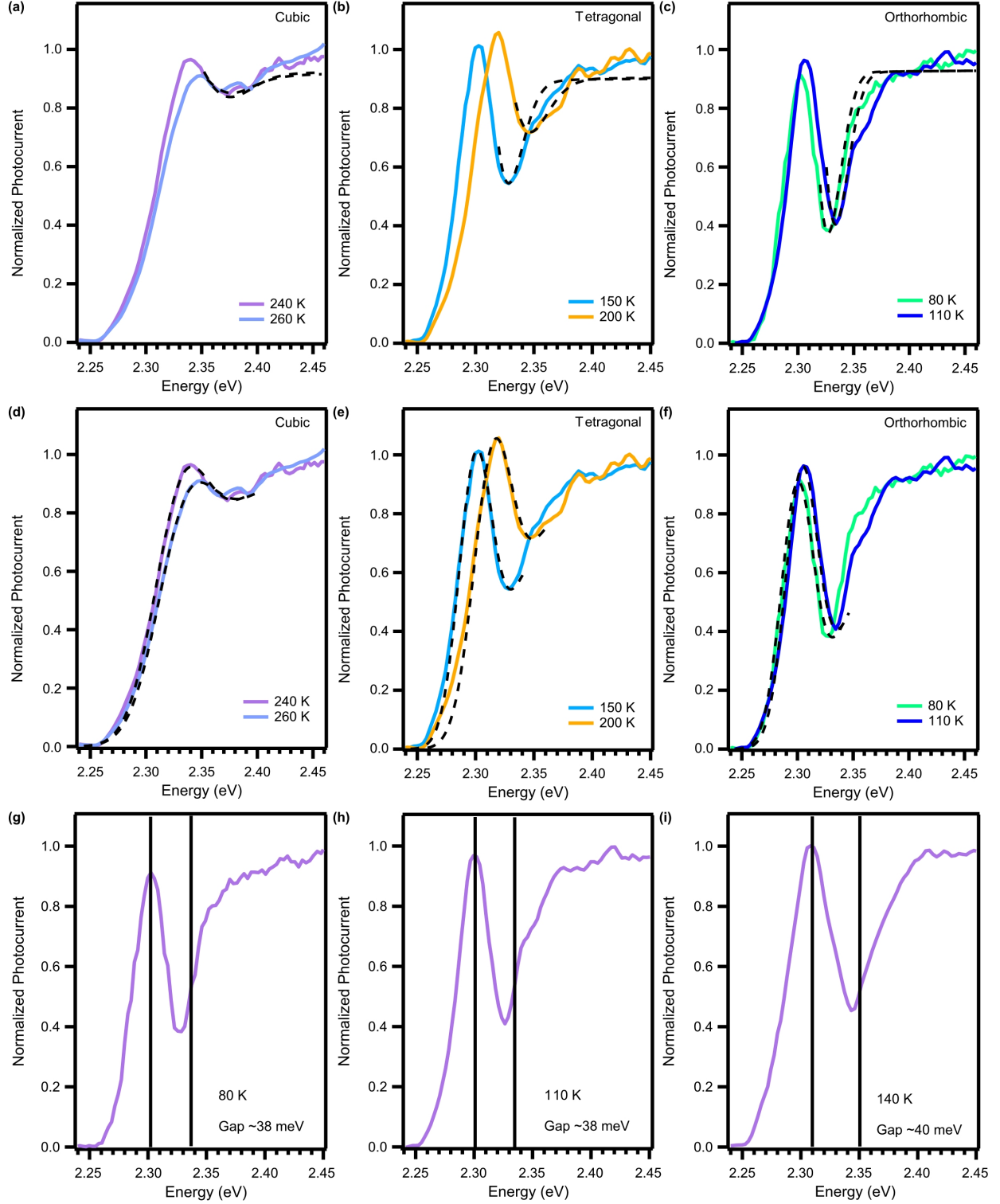


Figure S2: Various Elliott fittings. (a-c) High energy fit examples. (d-f) Low energy fit examples. (g-i) E_B estimated from the energy difference between the exciton peak and the half height of the continuum edge.

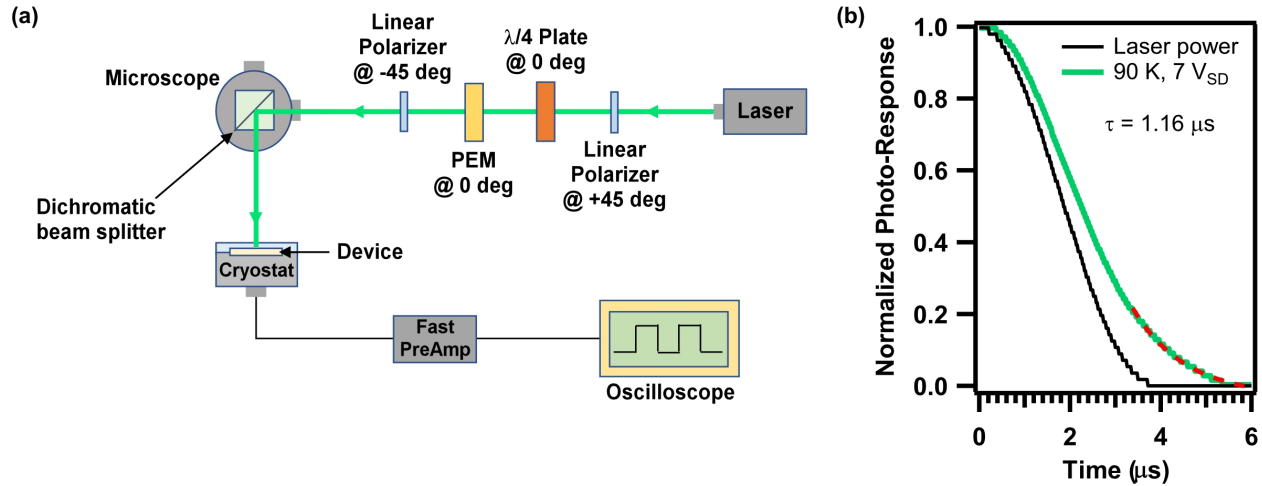


Figure S3: **Transient Photocurrent Measurement.** We use a combination of a photoelastic modulator (PEM), quarter waveplate, and two crossed linear polarizers as an optical chopper to modulate the light intensity at 50 kHz with a light intensity decay of about $1 \mu\text{s}$. A high-speed amplifier (Femto DHP-100) and a digital oscilloscope were used to measure the transient photocurrent. Time-resolved photocurrent (TRPC) measurements. (a) TRPC setup by using a photoelastic modulator (PEM) based chopper. (b) Transient photocurrent measurement at 90 K and $V_{\text{SD}} = 7 \text{ V}$. The black curve is the laser power change over time. The dashed red curve is the exponential fitting of the photocurrent decay after the light is completely turned off.

Temperature- and Field-Dependent Exciton Fraction

We calculate the fraction of excitons over the total photoexcited carriers (f_{ex}) in both MAPbI₃ and MAPbBr₃ (Fig. 2f in the main text). The Saha equation³ is used to calculate the exciton dissociation constant, $K(0) = np/n_x = \lambda^{-3}e^{-E_B/k_B T}$, where n_x is the exciton density, $\lambda = h/\sqrt{2\pi m_x^* k_B T}$ is the thermal deBroglie wavelength, and $m_x^* = m_e m_h / (m_e + m_h)$ is the effective mass of an exciton. The parameters used for the calculation are shown in the SI. The exciton fraction is then given by $f_{ex} = n_x / (n_x + n) = p / [K(0) + p]$ for p -type devices at moderate laser excitation intensity as used in our experimental conditions. The exciton fraction increases exponentially as temperature decreases and the additional abrupt increases are caused by the sudden change of exciton binding energy across the phase transitions. f_{ex} is larger in MAPbBr₃ and saturates at 100% at 80 K. In addition, we also calculate f_{ex} at the contact metal junction. Because of the large electric field (estimated to be 5 V/ μ m) in the depletion region, excitons are more easily dissociated into free carriers. The dissociation constant is enhanced by a factor of $K(E)/K(0) = \frac{J_1(2\sqrt{-2b})}{\sqrt{-2b}}$, where J_1 is the Bessel function of order one and $b = \frac{e^3 E}{8\pi\epsilon_r\epsilon_0 k_B^2 T^2}$.^{4,5}

We also plotted the free carrier fraction $f_c = 1 - f_{ex}$ in Fig. S4a. The free carrier fraction is about 10^{-2} at 80 K and 10^{-19} at 10 K. Such low free carrier concentrations at low temperatures indicate that the free carrier diffusion unlikely account for the observed nonlocal photocurrent. Furthermore, we performed additional SPCM measurements at 10 K, where the diffusion length remains extremely long (Fig. S4b). Hence, it is evident that excitons are responsible for the observed long diffusion lengths at low temperatures.

Table S1: Physical parameters used in the calculation of exciton fractions and scattering rates in MAPbBr₃. The values of the last five quantities (exciton binding energy, exciton Bohr radius, and the polaron radii) are calculated by using a polaronic exciton model.¹⁰ The γ values in the main text are calculated using the orthorhombic phase parameters. As the photocurrent decay length is determined by the minority carrier diffusion in absence of excitons, we used the electron (hole) polaron radius for p (n) type MAPbBr₃ (MAPbI₃).

Symbol	Physical meaning	Orthorhombic	Tetragonal	Cubic
m_e^*	electron effective mass ⁶	0.24	0.24	0.24
m_h^*	hole effective mass ⁶	0.30	0.30	0.30
m_x^*	exciton effective mass	0.13	0.13	0.13
ϵ_0	static dielectric constant ⁷	25	25	30
ϵ_∞	high frequency dielectric constant ⁸	4.4	4.4	4.4
$\hbar\omega_{LO}$ (meV)	LO phonon energy ⁹	8	15.3	15.3
E_B (meV)	exciton binding energy	40.5	25.9	23.6
a_0 (nm)	exciton Bohr radius	1.86	1.99	2.00
R_e (nm)	electron polaron radius	4.45	3.22	3.22
R_h (nm)	hole polaron radius	3.98	2.88	2.88
R_x (nm)	exciton polaron radius	5.98	4.32	4.32

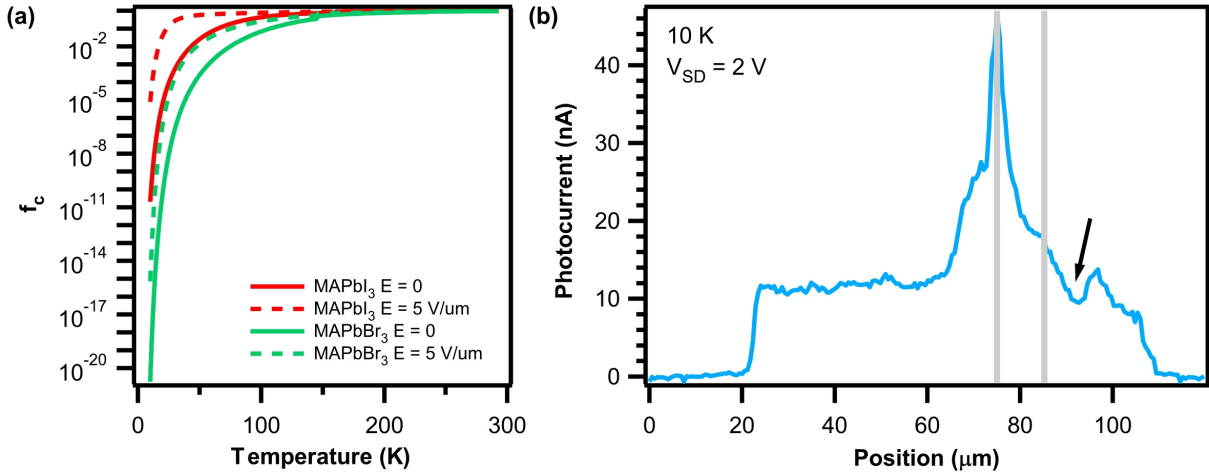


Figure S4: (a) Calculated free carrier fraction (f_c) as a function of temperature. f_c is less than 10^{-19} at 10 K. **(b)** Long photocurrent decay length is experimentally observed with SPCM at 10 K. Black arrow indicates the position of a surface crack that formed in the crystal likely due to the thermal expansion coefficient mismatch and the phase transition at the very low temperature, which caused a dip in the photocurrent.

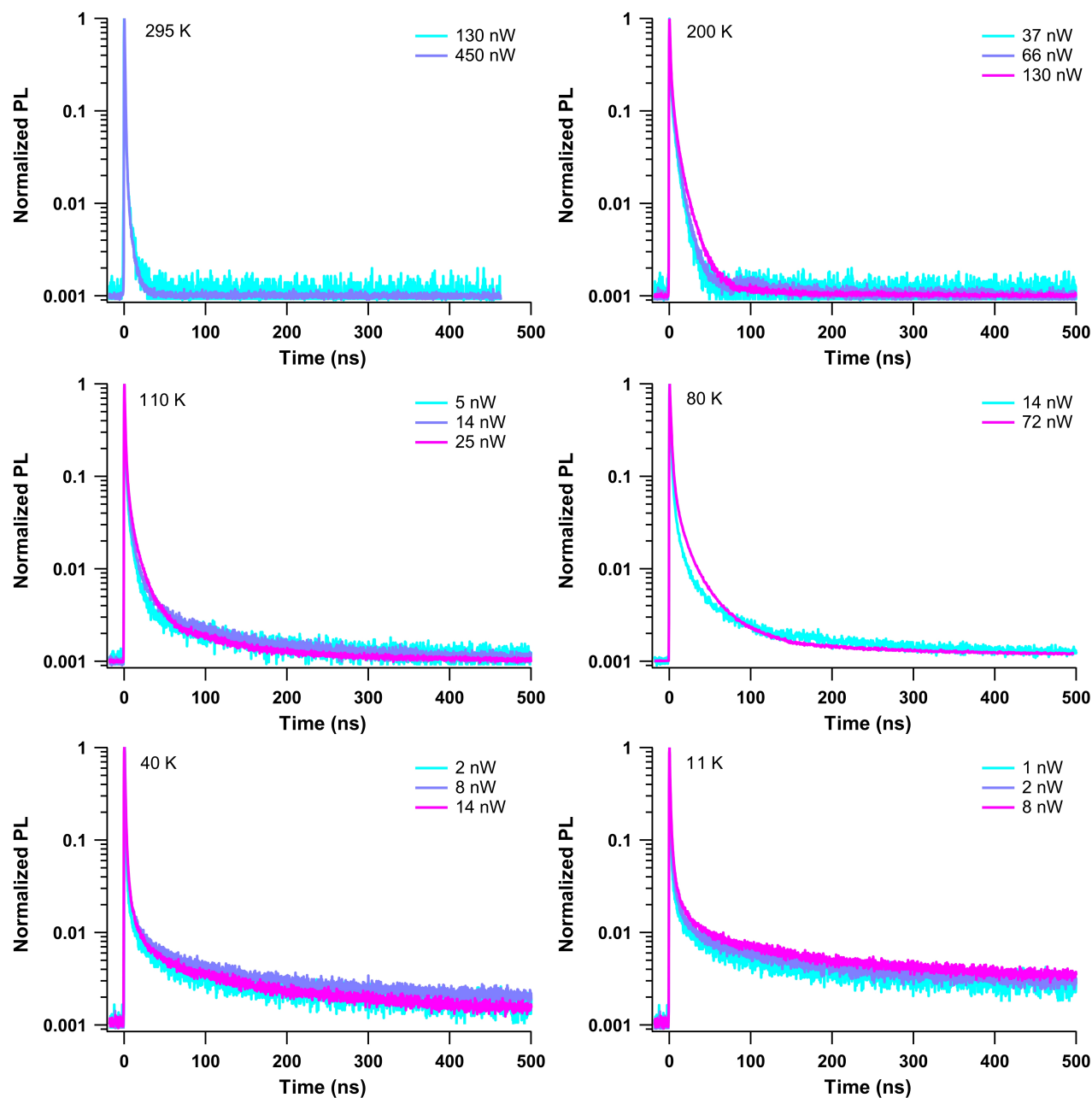


Figure S5: **Laser power dependence of time-resolved photoluminescence (TRPL) measurements at various temperatures.** TRPL lifetimes showed little to no power dependence across the full range of temperatures, indicating monomolecular recombination dominates in the intensity range used here ($0.13 - 57 \text{ W/cm}^2$). Lower intensities had to be used at low temperature due to rapidly increasing PL emission over-saturating the detection system.

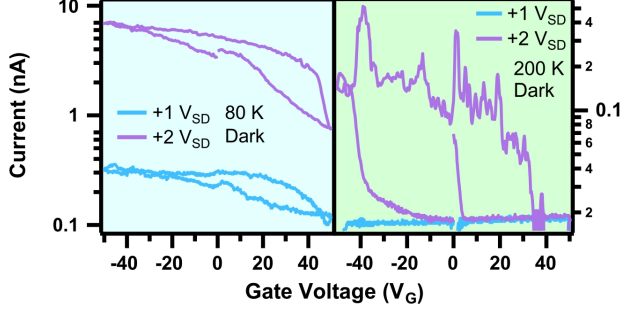


Figure S6: I - V_G plots from another device, showing typical p -type behavior that was observed in most samples. V_G is scanned at 2.5 V/s.

Exclusion of Exciton-Polariton Mechanism

PL spectra were taken from two representative microribbons with length of 15 and 60 μm , respectively. The short microribbon shows multiple PL peaks with energies in good agreement with that expected from the Fabry-Perot mode (Fig. S7). The peak separations in energy are expected to be 8-14 meV, as calculated by $\Delta E = \frac{hc}{2nL}$, where $L = 15 \mu\text{m}$ is the cavity length and n is the group refractive index of the polariton ($n = 3-5$) for a large cavity in MAPbBr₃ at the relevant wavelength range.¹¹ The non-linearity of the trend implies a polariton nature, rather than purely photons (Fig. S7 inset).

A similar feature (multiple PL peaks) is also observed in the 60 μm microribbon PL spectra (Fig. S8). However, the peaks are expected to be much closer together in energy for the Fabry-Perot mode along the long ribbon. The peak separations in energy are expected to be 2.1-3.4 meV for $L = 60 \mu\text{m}$ and $n = 3-5$. The discrepancy may be due to the thermal broadening of PL peaks and/or convolution of other cavity modes such as the Fabry-Perot mode from the width of the microribbon, which is much smaller. Therefore, exciton-polariton condensation unlikely accounts for the observed 100 μm photocurrent decay lengths in our microribbons without manufactured cavities.

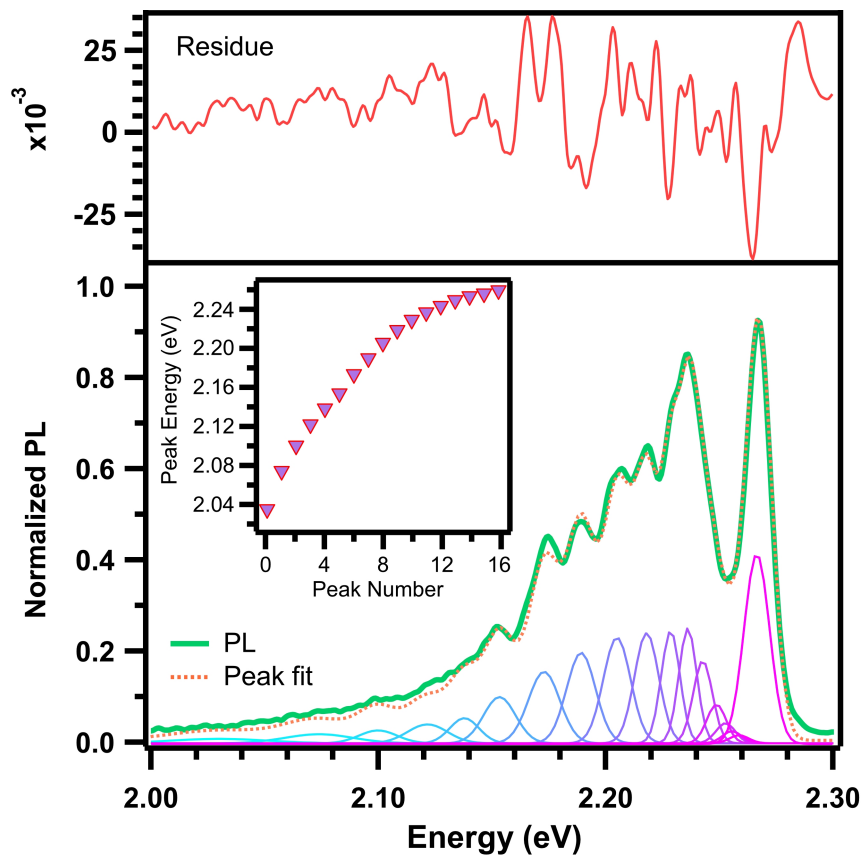


Figure S7: **PL spectra of a short microribbon sample.** microribbon sample, length of $\sim 15 \mu\text{m}$, with PL that displayed multi-peak features, resembling polariton behavior.¹¹ Multicolored peaks are Gaussian fitting components, scaled down for better viewing. The peak fit is the summation of the multicolored peaks with fit residue displayed above. Inset, peak energy of each multicolored peak used in fitting as a function of peak index number.

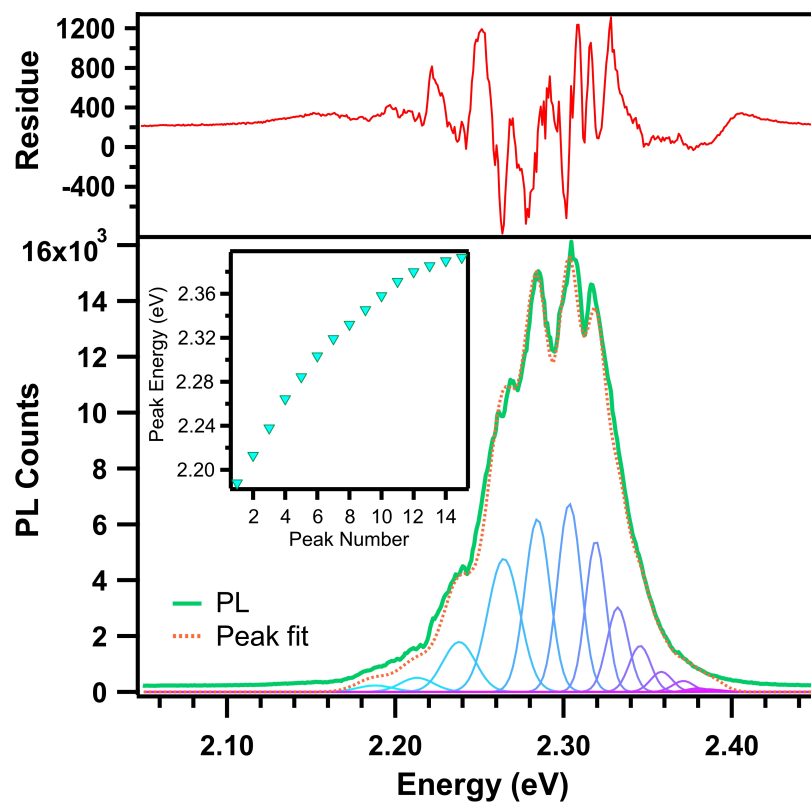


Figure S8: **PL spectra of a longer microribbon sample.** microribbon sample, length of $\sim 60 \mu\text{m}$, with PL that displayed multi-peak features.

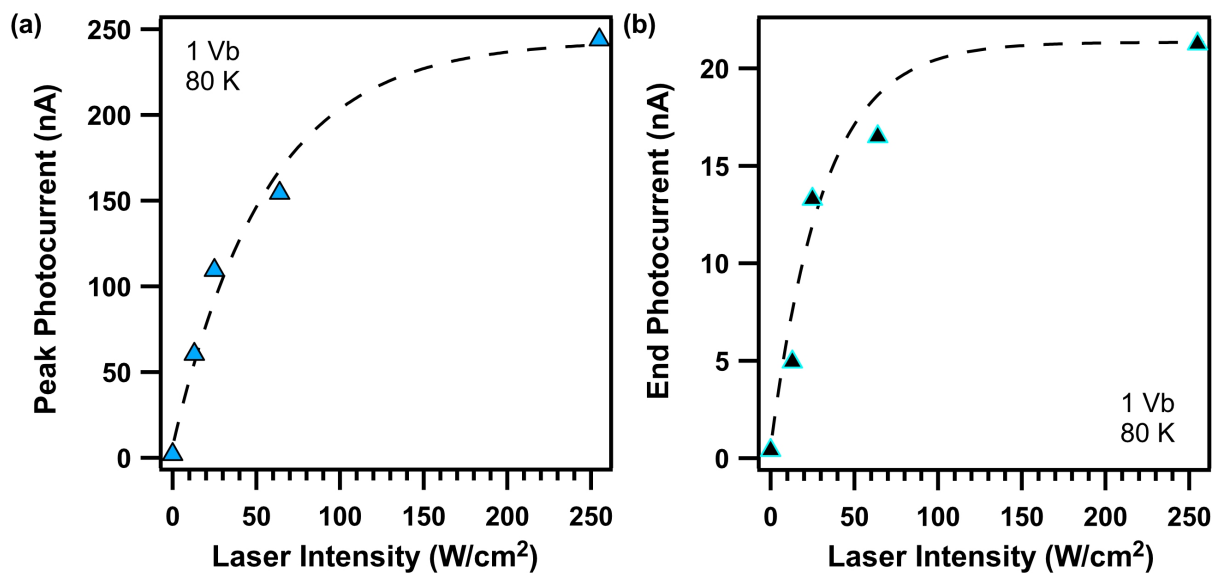


Figure S9: **Power-dependent photocurrent.** Photocurrent values extracted from the SPCM profiles at the contact (a) and the far end of the ribbon (b), respectively, as function of laser intensity at 80 K. The laser wavelength is at 500 nm. The non-linear power dependence indicates the bimolecular recombination dominates at the laser intensity used for SPCM.

References

- (1) Ruf, F.; Aygüler, M. F.; Giesbrecht, N.; Rendenbach, B.; Magin, A.; Docampo, P.; Kalt, H.; Hetterich, M. Temperature-dependent studies of exciton binding energy and phase-transition suppression in (Cs, FA, MA) Pb (I, Br) 3 perovskites. *APL Mater.* **2019**, *7*, 031113.
- (2) Chen, F.; Zhu, C.; Xu, C.; Fan, P.; Qin, F.; Manohari, A. G.; Lu, J.; Shi, Z.; Xu, Q.; Pan, A. Crystal structure and electron transition underlying photoluminescence of methylammonium lead bromide perovskites. *J. Mater. Chem. C* **2017**, *5*, 7739–7745.
- (3) D’innocenzo, V.; Grancini, G.; Alcocer, M. J.; Kandada, A. R. S.; Stranks, S. D.; Lee, M. M.; Lanzani, G.; Snaith, H. J.; Petrozza, A. Excitons versus free charges in organo-lead tri-halide perovskites. *Nat. Commun.* **2014**, *5*, 3586.
- (4) Tang, K. W.; Li, S.; Weeden, S.; Song, Z.; McClintock, L.; Xiao, R.; Senger, R. T.; Yu, D. Transport Modeling of Locally Photogenerated Excitons in Halide Perovskites. *J. Phys. Chem. Lett.* **2021**, *12*, 3951–3959.
- (5) Fuoss, R.; Accascina, F. *Electrolytic conductance*; Interscience Publishers, 1959.
- (6) Yamada, Y.; Mino, H.; Kawahara, T.; Oto, K.; Suzuura, H.; Kanemitsu, Y. Polaron Masses in $\text{CH}_3\text{NH}_3\text{PbX}_3$ Perovskites Determined by Landau Level Spectroscopy in Low Magnetic Fields. *Phys. Rev. Lett.* **2021**, *126*, 237401.
- (7) Soufiani, A. M.; Huang, F.; Reece, P.; Sheng, R.; Ho-Baillie, A.; Green, M. A. Polaronic exciton binding energy in iodide and bromide organic-inorganic lead halide perovskites. *Appl. Phys. Lett.* **2015**, *107*, 231902.
- (8) Melissen, S. T. A. G.; Labat, F.; Sautet, P.; Le Bahers, T. Electronic properties of $\text{PbX}_3\text{CH}_3\text{NH}_3$ ($X = \text{Cl}, \text{Br}, \text{I}$) compounds for photovoltaic and photocatalytic applications. *Phys. Chem. Chem. Phys.* **2015**, *17*, 2199–2209.
- (9) Wright, A. D.; Verdi, C.; Milot, R. L.; Eperon, G. E.; Pérez-Osorio, M. A.; Snaith, H. J.;

- Giustino, F.; Johnston, M. B.; Herz, L. M. Electron–phonon coupling in hybrid lead halide perovskites. *Nat. Commun.* **2016**, *7*, 11755.
- (10) Senger, R. T.; Bajaj, K. K. Optical properties of confined polaronic excitons in spherical ionic quantum dots. *Phys. Rev. B* **2003**, *68*, 045313.
- (11) Zhang, S.; Shang, Q.; Du, W.; Shi, J.; Wu, Z.; Mi, Y.; Chen, J.; Liu, F.; Li, Y.; Liu, M. et al. Strong exciton–photon coupling in hybrid inorganic–organic perovskite micro/nanowires. *Adv. Opt. Mater.* **2018**, *6*, 1701032.